

# Computational analysis of the effect of SOI vertical slot optical waveguide specifications on integrated-optic biochemical waveguide wensitivity

Hongsik Jung<sup>1,+</sup>

## Abstract

The effect of the specifications of a silicon-on-insulator vertical slot optical waveguide on the sensitivity of homogeneous and surface sensing configurations for TE and TM polarization, respectively, was systematically analyzed using numerical software. The specifications were optimized based on the confinement factor and transmission power of the TE-guided mode distributed in the slot. The waveguide sensitivities of homogeneous and surface sensing were calculated according to the specifications of the optimized slot optical waveguide.

**Keywords :** Slot optical waveguide, Integrated optical biochemical sensor, Label-free, Confinement factor, Waveguide sensitivity, Homogeneous sensing, Surface sensing.

## 1. INTRODUCTION

Over the past 20 years, integrated-optical biochemical sensors have been recognized as excellent tools for detecting analytes in biochemical, health and environmental applications, and many studies have been conducted. Integrated-optical sensors can monitor analytes by utilizing various physical parameters such as intensity, wavelength, phase, and polarization of light waves as a conversion medium, and have unique features such as remote sensing, multi-sensing, and robustness to electromagnetic interference. Furthermore, a variety of well-developed passive and active optically integrated components can be utilized in sensors [1-3].

Biochemical sensors based on light waves are largely divided into label-based and label-free sensors. For the former, the presence of a specific molecule can be measured as a quantified value by detecting a target molecule or a bio-recognizable molecule through a fluorescence or light absorption marker. However, it requires complex liquid handling, labeling processes, relatively long analysis times, bulky measuring equipment, and

skilled professionals. On the other hand, if integrated optic waveguide devices are utilized, various label-free sensors can be effectively implemented. For label-free biochemical sensors, the concentration change of a chemical analyte to be sensed affects the effective refractive index of the propagating modes, which is measured in different ways, according to the sensor architecture. The effective index change is produced either by a change in the cover medium refractive index in the process called “homogeneous sensing,” as shown in Fig. 1(a) or by a change in the thickness of an ultra-thin layer of receptor molecules that are immobilized on a waveguide surface in a process called “surfacing sensing,” as shown in Fig. 1(b). As the label-free sensing method can be used to monitor the refractive index of a target molecule in real time, it has been employed in biochemical sensors that can be used at the point of care, such as those that detect DNA sequenced by hybridization and antigen-antibody reactions, and for measuring pollutant concentrations in water. Considerable research has been conducted on label-free sensing [4,5].

Integrated-optical sensors based on channel optical waveguides has important advantages over bulk optical devices and optical fiber-based sensors. Because the channel optical waveguide uses standard photolithography fabrication technology, it is low cost and easy to manufacture, thus, mass production is possible. Furthermore, multiple optical waveguide-based sensors can be integrated on a single chip so that multiple analytes can be detected simultaneously. Moreover, it is possible to use well-established microelectronics fabrication processes (i.e., CMOS technology) to fabricate the sensors which can be integrated with

---

<sup>1</sup>Dept. of Electronic & Electrical Engineering, College of Science & Technology, Hongik University  
Hongik University, 2639, Sejong-ro, Jochiwon, Sejong 30016, Korea  
<sup>+</sup>Corresponding author: [hsjung@hongik.ac.kr](mailto:hsjung@hongik.ac.kr)  
(Received: Oct. 25, 2021, Accepted: Nov. 22, 2021)

This is an Open Access article distributed under the terms of the Creative Commons Attribution Non-Commercial License(<https://creativecommons.org/licenses/by-nc/3.0/>) which permits unrestricted non-commercial use, distribution, and reproduction in any medium, provided the original work is properly cited.

electronic C-MOS chip modules, thus miniaturizing the sensor to the chip level [6,7].

Most silicon-based integrated optical biosensors have been implemented in various forms using ridge- or rib-optical waveguides utilizing high-index contrast material systems such as Si/SiO<sub>2</sub> or Si<sub>3</sub>N<sub>4</sub>/SiO<sub>2</sub>. [8,9] Although the optical waveguides manufactured in this way strongly confine most of the light waves to the core of a high-refractive-index material (i.e., core) surrounded by a low-refractive-index material (i.e., cladding) by total internal reflection (TIR), some light waves called evanescent wave also exist in the cladding area. Therefore, when the cladding area where a weak evanescent wave exists is composed of a biochemical analyte, the effective refractive index of the fundamental mode, which has a lot of influence on the intensity, phase, and polarization of a light wave, is affected by the evanescent wave; however, because the evanescent wave itself is very weak, it is difficult to expect a large degree of sensitivity.

After Almeida et al. proposed a slot optical waveguide structure in 2004, considerable amount of research using it for biochemical sensors has been conducted with high interest for the past 15

years. [10-13] In the case of slot optical waveguides, a high proportion of the fundamental mode propagates through the low-refractive-index slot region between the two high-refractive-index rails. In other words, from a quantitative point of view, a significant portion of the mode exists in the slot owing to the continuity boundary condition of the electric field at the rail-slot interface. Therefore, when the slot is filled with a biochemical analyte with a smaller refractive index than the rail, a stronger interaction occurs with the fundamental mode propagating through the slot, and excellent sensing characteristics can be expected. The slot optical waveguide is divided into vertical slot [14] and horizontal slot [15] optical waveguide structures; furthermore, vertical and horizontal slot optical waveguides are modified into ridge-slot [16] and loaded-slot [17] structures.

Various optical integrated devices have been fabricated and studied using slotted optical waveguides, such as micro-ring resonators [18,19], optical modulators [20,21], electrically pumped light emitting devices [22], directional couplers [23], all-optical logic gates [24], and beam splitters [25]. Moreover, various numerical method-based modal analyses devoted to studying the influence of slot waveguide geometric parameters on the optical power fraction confined in the slot region have also been carried out [26,27].

Therefore, in this study, the effect of the specifications of the vertical slot optical waveguide (i.e., the width of the slot, and the width and height of the rail) on the field distribution and intensity of the fundamental TE or TM mode was systematically examined through the value of the confinement factor and transmission power. The specifications of the optimized slot optical waveguide structure were derived, and then the sensing capability (waveguide sensitivity) based on the optimized specification was examined for homogeneous and surface sensing [28]. In Chapter 2, the TE and TM modal analytical expressions are theoretically examined by applying the Maxwell wave equation to the vertical-slot optical waveguide. In Chapter 3, the effects of the specifications of the vertical-slot optical waveguide on the modal distribution and transmission power was systematically simulated using the FIMMWAVE and FIMMPROP software of Photon Design [29, 30]. In Chapter 4, with a focus on optimized specifications, the waveguide sensitivities for homogeneous and surface sensing were evaluated based on the changes in the effective refractive indices of the fundamental TE and TM modes due to changes in the specific ranges of the refractive indices and thicknesses of the receptor of various analytes (water, isopropanol, ethylene glycol, and sodium chloride). The conclusions are presented in Chapter 5.

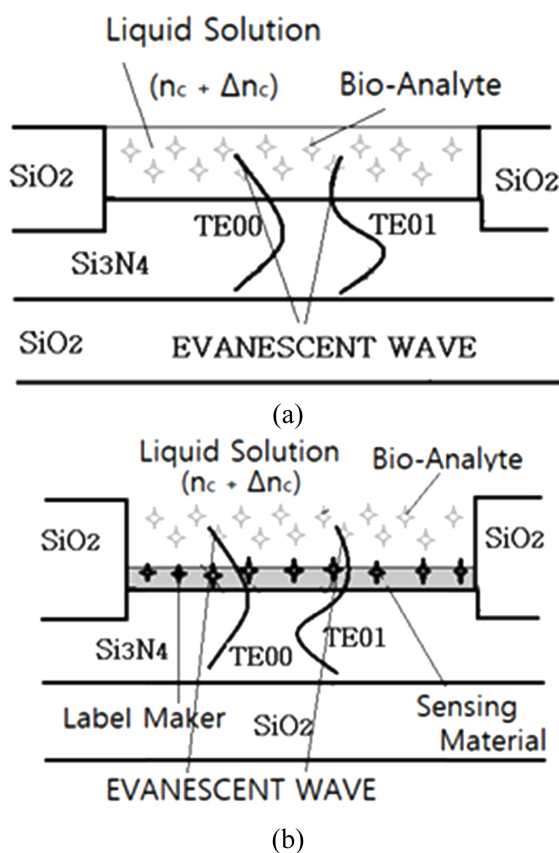


**Fig. 1.** Two biosensor schematics showing the concept of an evanescent wave in an integrated-optical waveguide for (a) homogeneous (bulk) sensing and (b) surface sensing.

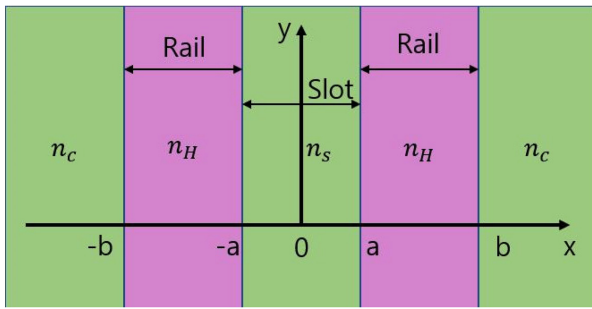


**Fig. 2.** Cross-section of a vertical slot optical waveguide for the analysis of optical mode.

## 2. MODAL ANALYSIS OF THE VERTICAL SLOT OPTICAL WAVEGUIDE

Fig. 2 show a two-dimensional cross-section of a slot optical waveguide composed of rails satisfying the  $n_H > n_s$  condition on both sides of the slot with a refractive index  $n_s$ . The phenomenon in which the TE and TM modal fields of the light wave in the slot area are more distributed than those in the rail area, and are guided along the slot is analyzed by Maxwell's wave equations, Eq. (1), and the boundary conditions in Eq. (2) and Eq. (3) as shown below, to ensure that the mode field is continuous at the two boundaries to induce transverse electric (TE) mode,  $E_y(x)$  and transverse magnetic (TM) mode,  $E_x(x)$ . By utilizing the field distribution of the induced mode, the ratio of the mode distributed in the slot is quantitatively evaluated by a confinement factor. Descriptions of the development of equations related to mode derivation can be found in many papers; therefore, formula development has been described implicitly in this paper [31-33]. Since the field distribution of the mode in the slot and rail region varies depending on whether the distribution profile is a hyperbolic-cosine or hyperbolic-sine function, the mathematical expressions of the field distribution are interpreted as follows under the following assumption:  $n_H > n_c \geq n_s$  ;

$$\frac{d^2 E_y}{dx^2} + (k_0^2 n^2 - \beta^2) E_y = 0 \quad \text{for TE} \quad (1-1)$$

$$\frac{d^2 E_x}{dx^2} + (k_0^2 n^2 - \beta^2) E_x = 0 \quad \text{for TM} \quad (1-2)$$

The boundary conditions (2) and (3) for the TE and TM modes, respectively, are as follows:

$$E_{y1}(a) = E_{y2}(a) \quad (2-1)$$

$$\left. \frac{\partial E_{y1}(x)}{\partial x} \right|_{x=a} = \left. \frac{\partial E_{y2}(x)}{\partial x} \right|_{x=a} \quad (2-2)$$

$$n_1^2 E_{x1}(a) = n_2^2 E_{x2}(a) \quad (3-1)$$

$$\left. \frac{\partial E_{x1}(x)}{\partial x} \right|_{x=a} = \left. \frac{\partial E_{x2}(x)}{\partial x} \right|_{x=a} \quad (3-2)$$

Therefore, the general TE and TM mode field distributions that satisfy Eqs. (1), and the propagation constants defined in each region of the slot, rail, and clad are expressed as follows:

$$r_1 = \sqrt{\beta^2 - k_0^2 n_s^2} \quad (4-1)$$

$$r_2 = \sqrt{k_0^2 n_H^2 - \beta^2} \quad (4-2)$$

$$r_3 = \sqrt{\beta^2 - k_0^2 n_c^2} \quad (4-3)$$

$$E_y(x) = \begin{cases} A_1 \cosh(r_1 x) & \text{if } |x| < a \\ A_2 \cos(r_2(|x| - a)) + B_2 \sin(r_2(|x| - a)) & \text{if } a < |x| < b \\ A_3 e^{-r_3(|x| - b)} & \text{if } b < |x| \end{cases} \quad (5)$$

When the TE and TM mode boundary conditions (2) and (3) are applied to Eqs. (5), the TE and TM mode distributions in the form of hyperbolic-cosines are derived as shown in Eq. (6) and (7), respectively [22].

$$E_y(x) = \begin{cases} A_1 \cdot \cosh(r_1 x) & \text{if } |x| < a \\ A_1 \cosh(r_1 a) \cos(r_2(|x| - a)) + \frac{r_1}{r_2} \sinh(r_1 a) \sin(r_2(|x| - a)) & \text{if } a < |x| < b \\ A_1 \cdot \{ \cosh(r_1 a) \cos(r_2(|b| - a)) + \frac{r_1}{r_2} \sinh(r_1 a) \sin(r_2(|b| - a)) \} \cdot e^{-r_3(|x| - b)} & \text{if } b < |x| \end{cases} \quad (6)$$

$$E_x(x) = \begin{cases} \frac{A_1}{n_s} \cdot \cosh(r_1 x) & \text{if } |x| < a \\ A_1 n_s \cdot \{ \frac{1}{n_H} \cosh(r_1 a) \cos(r_2(|x| - a)) + \frac{r_1}{r_2 n_s^2} \sinh(r_1 a) \sin(r_2(|x| - a)) \} & \text{if } a < |x| < b \\ \frac{A_1 n_s}{n_c^2} \cdot \{ \cosh(r_1 a) \cos(r_2(|b| - a)) + \frac{r_1 n_H^2}{r_2 n_s^2} \sinh(r_1 a) \sin(r_2(|b| - a)) \} \cdot e^{-r_3(|x| - b)} & \text{if } b < |x| \end{cases} \quad (7)$$

On the other hand, if the field distribution is assumed to be hyperbolic-sine and the boundary conditions (2) and (3) are applied to Eq. (5), then, the TE and TM mode distributions, as shown in Eq. (8) and (9), respectively, can be obtained [28].

$$E_y(x) = \begin{cases} \frac{A_1}{n_c^2} \cdot \sinh(r_1 x) & \text{if } |x| < a \\ A_1 \cdot \frac{x}{|x|} \{ \sinh(r_1 a) \cos(r_2(|x| - a)) + \frac{r_1}{r_2} \cosh(r_1 a) \sin(r_2(|x| - a)) \} & \text{if } a < |x| < b \\ A_1 \cdot \frac{x}{|x|} \{ \sinh(r_1 a) \cos(r_2(|b| - a)) + \frac{r_1}{r_2} \cosh(r_1 a) \sin(r_2(|b| - a)) \} \cdot e^{-r_3(|x| - b)} & \text{if } b < |x| \end{cases} \quad (8)$$

$$\begin{aligned}
 E_x(x) &= \frac{A_1}{n_s} \cdot \sinh(r_1 x) && \text{if } |x| < a \\
 &= A_1 n_s \cdot \frac{x}{|x|} \left\{ \frac{1}{n_H^2} \sinh(r_1 a) \cos(r_2(|x| - a)) + \right. \\
 &\quad \left. \frac{r_1}{r_2 n_s^2} \cosh(r_1 a) \sin(r_2(|x| - a)) \right\} && \text{if } a < |x| < b \\
 &= A_1 n_s \cdot \frac{x}{|x|} \sinh(r_1 a) \cos(r_2(|b| - a)) + \\
 &\quad \frac{r_1 n_H^2}{r_2 n_s^2} \cosh(r_1 a) \sin(r_2(|b| - a)) \left. \right\} \cdot e^{-r_3(|x| - b)} && \text{if } b < |x|
 \end{aligned} \tag{9}$$

Therefore, when the rail refractive index ( $n_H$ ) is greater than the slot refractive index ( $n_s$ ), it can be confirmed that the field distribution of the mode in the slot is significantly larger based on the relationship  $|E_s / E_H| = (n_H / n_s)^2$ . In addition, because the slot width is similar to the attenuation length of the field, the strength of the mode field in the slot is relatively high throughout the slot.

### 3. OPTIMIZATION OF THE SLOT OPTICAL WAVEGUIDE

In order to apply the slotted optical waveguide to a biochemical sensor, a large field distribution of the fundamental mode in the slot area is needed, as it will have a great effect on the optical properties of the analyte, improving sensitivity. Therefore, it is important to determine the specifications of the slot optical waveguide so that a large portion of the field of the fundamental mode can be transmitted through the slot within the refractive index range of the analyte. The Effect of slot width, rail thickness, and height on the field distribution formed in the slot was systematically examined through the confinement factor and transmission power of the TE mode by numerical analysis using the FIMMWAVE and FIMMPROP software [29,30]. The optimization of slot waveguide specifications was carried out mainly in TE mode because the TE mode is significantly more sensitive to the medium refractive index change than the TM mode, according to data reported in the references.

#### 3.1 Investigation of the Modal Confinement Factor

In the optical waveguide structure as shown in Fig. 3, the analytes filled in the slot were assumed to be H<sub>2</sub>O ( $n_s = 1.31$ ), isopropanol ( $n_s = 1.377$ ), ethylene glycol ( $n_s = 1.505$ ), and sodium chloride ( $n_s = 1.5443$ ), and then computational analysis was performed. First, the width and height of the rail were set to 200 nm and 320 nm, respectively, and the ratio of the fundamental mode distributed to the slot was examined through a confinement factor defined by Eq. (10) while increasing the width of the slot

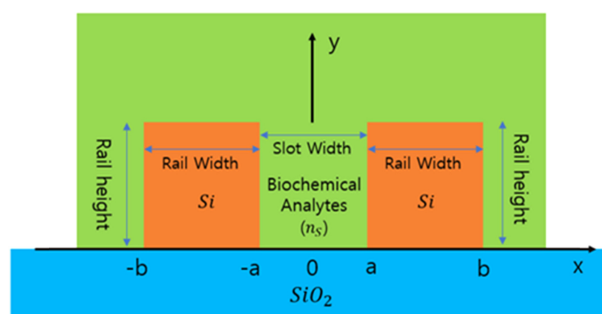


Fig. 3. Cross-sectional schematic of the vertical slot optical waveguide for computational analysis.

from 40 nm to 200 nm.

$$\Gamma = \frac{\iint_{slot} Re(E \times H^*) \cdot z dx dy}{\iint_{total} Re(E \times H^*) \cdot z dx dy} \tag{10}$$

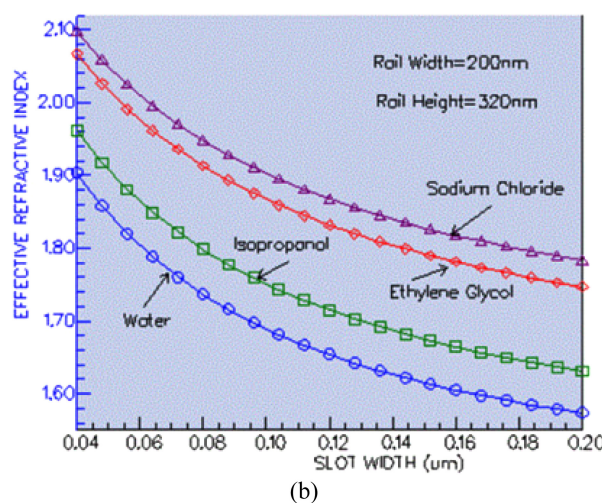
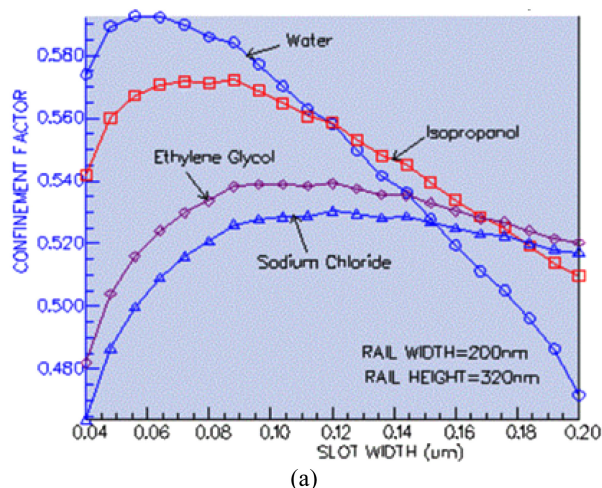


Fig. 4. Change in the (a) confinement factor and (b) effective refractive index of TE mode in the slot region with an increase in the slot width for various analytes (rail width = 200 nm; rail height = 320 nm).

Fig. 4(a) shows the tendency of the overall confinement factor to increases as the slot width increases and then decrease after a certain maximum value. In the case of H<sub>2</sub>O and isopropanol, the confinement factor at a slot width of approximate 60 nm shows a high value of about 0.58 or more, and then decreases rapidly. On the other hand, ethylene glycol and sodium-chloride show a flat maximum value for widths in the range of 100 to 120 nm and then gradually decrease. As can be seen in Fig. 4(a), the confinement factor decreases after the maximum values because the width of the slot widens, as a result, a small portion of the incident light wave begins to be transmitted through the rail acting as an SOI optical waveguide rather than a slot. Furthermore, as the width of the slot increases, the effective refractive index of the fundamental mode decreases, as shown in Fig. 4(b), because a large portion of light is confined within the slot, which has a low refractive index.

To examine the effect of the rail width on the confinement factor, the slot width and height were set to 120 nm and 320 nm, respectively, the rail width was gradually increased within the range of 140 to 240 nm, and the confinement factor was calculated for the aforementioned analytes. As shown in Fig. 5, as the rail width increases, the confinement factor tends to increase until the rail width is 180-210 nm. Until the rail width reaches the appropriate width, it cannot sufficiently serve as the strip optical waveguide, and then, from the amount of light confined to the slot, the amount of light that escapes to the rail is small. Therefore, the confinement factor increases. On the other hand, when the rail width is increased beyond the optimal width and the rail itself begins to act as a strip optical waveguide, the confinement factor starts to decrease again because the light waves confined to the

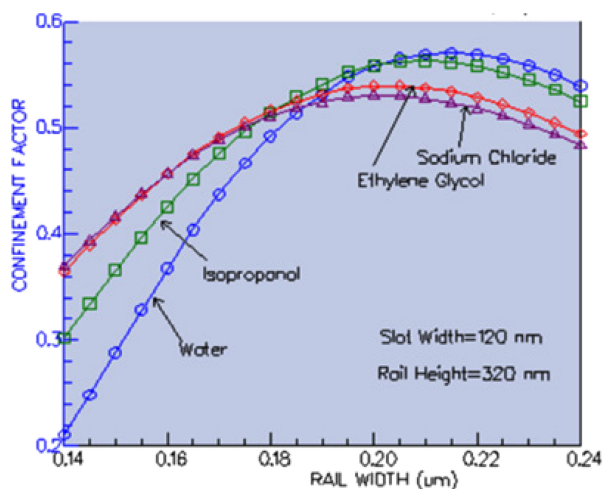


Fig. 5. Change in the confinement factor of the TE mode in slot region with an increase in the rail width for various analytes (slot width = 120 nm; rail height = 320 nm).

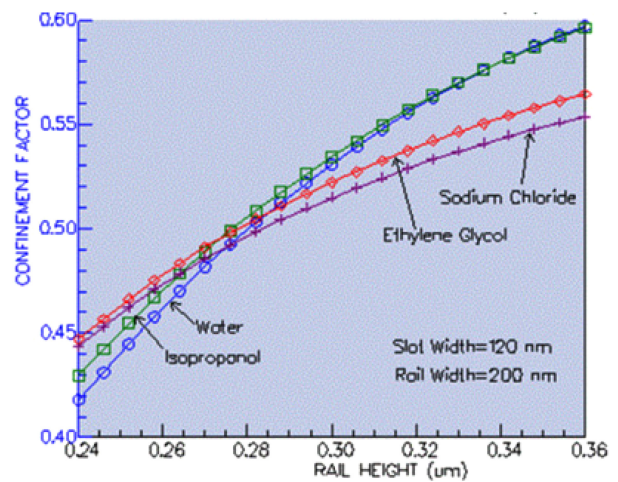


Fig. 6. Change in the confinement factor of the TE mode in the slot region as the rail height is increased for various analytes (slot width = 120 nm; rail width = 200 nm).

slot can be transmitted through the rail.

In order to examine the effect of the rail height on the light wave confinement factor, the rail and slot widths were set to 200 nm and 120 nm, respectively, the rail height was increased within the range of 240 nm to 360 nm, and the amount of light waves confined to the slot was examined as the confinement factor. Fig. 6 shows that, as the height of the rail increases, the confinement factor increases. This indicates that, the higher the rail height, the more difficult it is for the light waves confined to the slot to escape to the upper cladding region; as a result, the confinement coefficient increases. However, in the manufacturing process of the slotted optical waveguide, it is desirable to determine an appropriate height, given the difficulty of the etching process, its

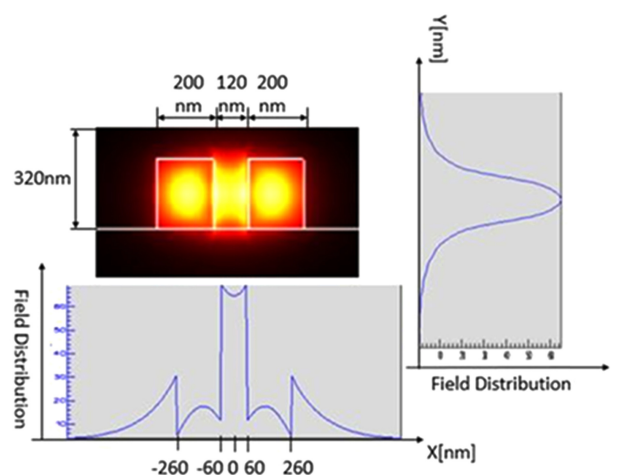


Fig. 7. Calculated two- and one-dimensional mode distributions for the  $E_y(x, y)$ ,  $E_y(x, 0)$  and  $E_y(0, y)$  of the TE fundamental mode in the slot waveguide.

processing time, and its cost. After consulting various references [16-19], a height of approximately 320 nm was estimated as an appropriate height.

Therefore, based on the results of the previous computational analysis, the rail width, rail height, and slot width of the optimized slot optical waveguide in the 1.5 μm wavelength range were set at 200 nm, 320 nm and 120 nm, respectively. Fig. 7 shows the two-dimensional field distribution and the field components corresponding to each direction of the x and y axis for the TE mode  $E_y(x)$ . As expected, the intensity of the mode field was strongly distributed in the slot, and the confinement factor was calculated to be over about 0.56. In SOI and  $\text{Si}_3\text{N}_4$  ridge or rib optical waveguide structures, weak evanescent waves appearing in the upper cladding contribute to sensing; however, in slot optical waveguides, more than 50% of the fundamental mode field propagates through the slot, and excellent sensing performance can be expected.

### 3.2 Investigation of the Transmission Power

Computational analysis of the normalization transmission power of the slot optical waveguide with a 5000 μm channel length was then performed, focusing on the previous-derived optimized specifications. First, the rail width and height were set to 200 nm and 320 nm, respectively, and the result, as shown in Fig. 8, was obtained through transmission power analysis while varying the slot width in the range of 20–180 nm. As the slot width increased, the transmission power increased until it reached the maximum power and then decreased. As the refractive index of the analyte increased, the slot width corresponding to the

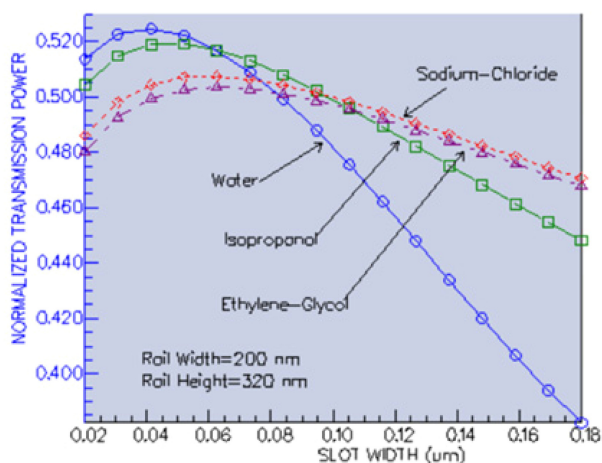


**Fig. 8.** Change in the normalized transmission power of the TE mode in the slot region with an increase in the slot width for various analytes (rail width = 200 nm; rail height = 320 nm).

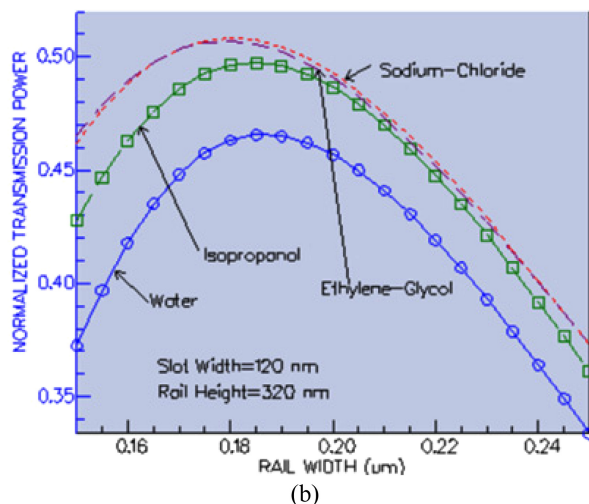
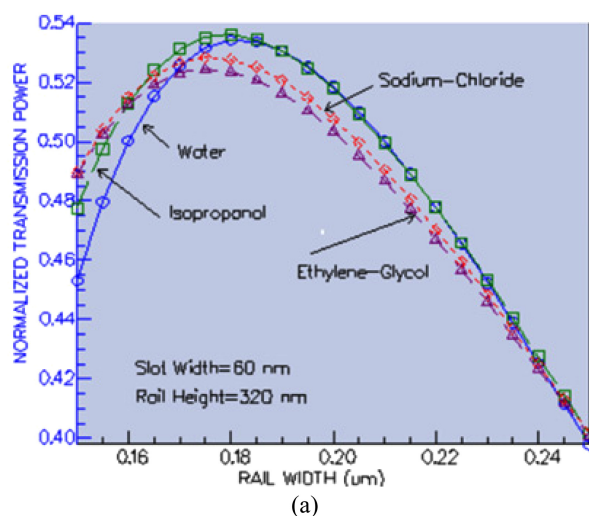


**Fig. 9.** Change in the normalized transmission power of the TE mode in the slot region with an increase in the rail width for various analytes and slot widths (a) 60 nm and (b) 120 nm (rail height = 320 nm).

maximum power tended to increase. Overall, the graph shows a trend very similar to that shown in Fig. 5, which was obtained based on the confinement factor.

In succession, the change in transmission power was analyzed computationally, as shown in Fig. 9, while increasing the rail width for slot widths of 60 nm and 120 nm. The maximum transmission power was obtained at a rail width of approximate 185 nm for both slot widths, which was shorter by approximately 20 nm than the optimized value derived based on the confinement factor, as shown in Fig. 5, but showed a very similar trend overall.

Finally, we set the slot widths to 60 nm and 120 nm and the rail widths to 200 nm, and analyzed the transmission power while increasing the rail height to obtain the results shown in Fig. 10. Regardless of the value of the refractive index of the analytes, the transmission power tended to increase as the rail height increased, and

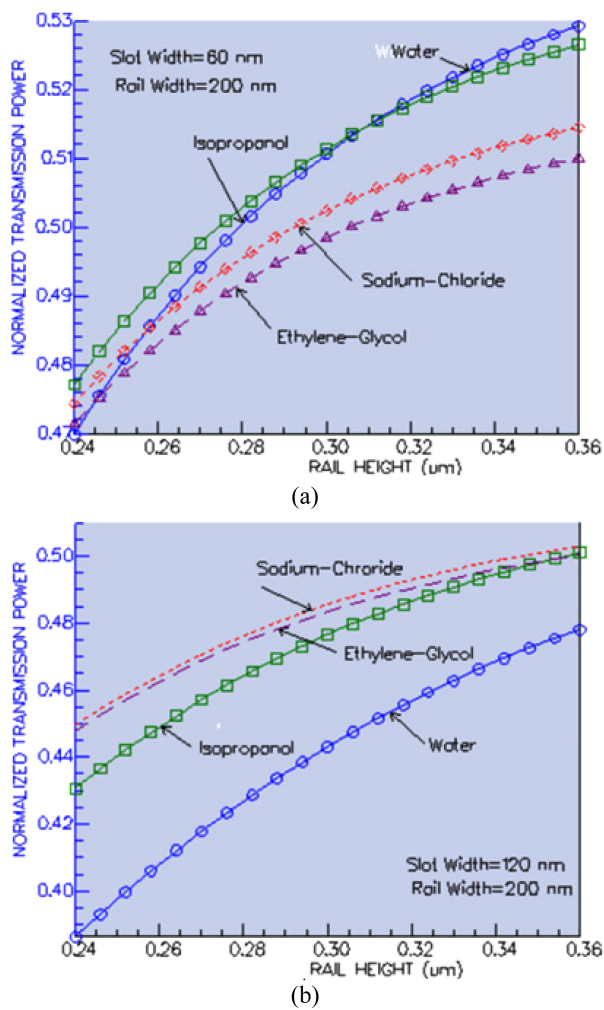


**Fig. 10.** Change in the normalized transmission power of the TE mode in the slot region with an increase in the rail height for various analytes and slot widths (a) 60 nm and (b) 120 nm (rail width = 200 nm).

it was confirmed that the increase slowed as the rail width increased. It also showed a very similar trend to that shown in Fig. 6.

#### 4. EVALUATION OF THE WAVEGUIDE SENSITIVITY

##### 4.1 Waveguide Sensitivity

Various figures of merit, such as sensitivity, limit of detection, selectivity, reproducibility, stability, and resolution, are widely used to evaluate sensor performance. Among these indicators, the sensitivity of a sensor is one of its most important characteristics. In particular, the sensitivity of an optical waveguide-based sensor consists of the optical waveguide sensitivity ( $S_w$ ) and the

architecture sensitivity ( $S_a$ ). The former reflects the effect of the change in the analyte refractive index or binding thickness on the variation in the effective refractive index of the mode. The effective refractive index of a waveguide mode is not a directly measurable quantity; therefore, it must be determined from a quantity that can be readily detected. To estimate the effective refractive index, a device with photonic sensing architecture is employed. Such devices can be broadly categorized into two different types: interferometric devices such as Mach-Zehnder interferometers, Young interferometers, and multimode interferometers, and resonant devices such as ring resonators and Fabry-Perot resonators. In devices with interferometric architectures, the variations of effective refractive index are related to optical phase shifts,  $\Delta\phi$  whereas in those with resonant architectures they are related to a resonant wavelength changes,  $\Delta\lambda$ .

In evanescent field sensors, the waveguide sensitivity is determined by the strength of the interactions between matter and the fraction of light in solution or at the surface. According to the status of the target molecules, two specific types of sensitivities, as mentioned in the introduction (refer to Fig. 1), are defined in biochemical sensing applications: (i) homogeneous (or bulk) sensitivity ( $S_{wh}$ ), which considers the refractive index changes in the waveguide's entire cladding; and (ii) surface sensitivity ( $S_{ws}$ ), which assesses refractive index changes within the first few tens to hundreds of nanometers above the surface. Homogeneous sensitivity is defined as the slope of the phase (or wavelength) shift versus the change in the refractive index. Therefore, the overall photonic device sensitivity  $S$  for the interferometric configuration can be defined as

$$S = S_a S_{wh} = \frac{\partial \phi}{\partial n_{eff}} \cdot \frac{\partial n_{eff}}{\partial n_a} = \frac{2\pi}{\lambda_0} \cdot L \cdot \frac{\partial n_{eff}}{\partial n_a} \quad (11)$$

where  $\lambda_0$  is the incident light wavelength,  $L$  is the interaction length, and  $n_a$  is the refractive index of the analyte (i.e., cover material) [34,35]. The sensitivity of the resonant configuration can also be defined as

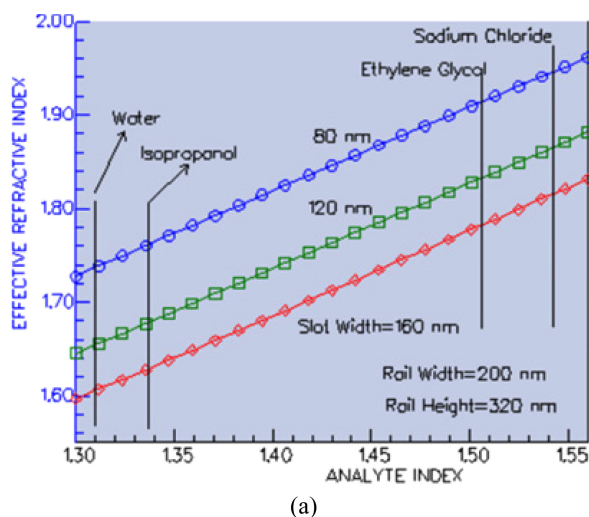
$$S = S_a S_{ws} = \frac{\partial \lambda_r}{\partial n_{eff}} \cdot \frac{\partial n_{eff}}{\partial t_a} = \frac{\lambda_0}{n_g} \cdot \frac{\partial n_{eff}}{\partial t_a} \quad (12)$$

where  $\lambda_r$  is the resonant wavelength,  $n_g$  is the waveguide group index, and  $t_a$  is the analyte thickness. Therefore, in this study, we focused on the effects of slot optical waveguide specifications on the waveguide sensitivity of homogeneous sensing and surface sensing. The sensitivity mentioned hereafter refers to the sensitivity of the waveguide.

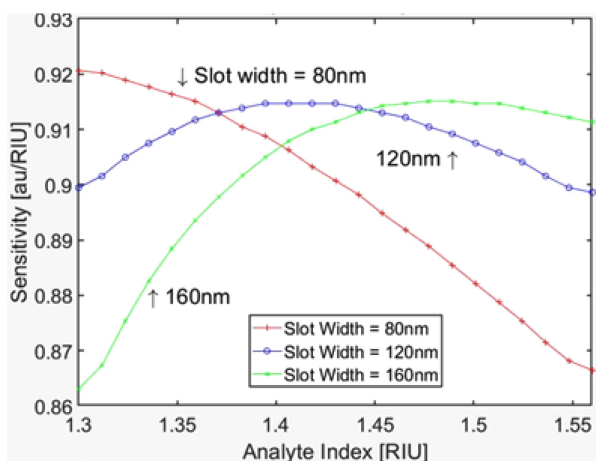
### 4.2 Homogeneous Sensing

In the optimized slot optical waveguide, the extent to which the effective refractive index ( $n_{eff}$ ) of the fundamental mode was affected by the change in the analyte refractive index ( $n_a$ ) was examined through computational analysis, and the sensitivity was evaluated.

First, the rail width and height of the slot optical waveguide were set to 200 nm and 320 nm, respectively, and the change in the effective refractive index of the fundamental mode was analyzed within the range of 1.3 to 1.55 of the index of the analyte for slot widths of 80 nm, 120 nm, and 160 nm. As shown in Fig. 11(a), as the refractive index of the analyte increases, the effective refractive index of the fundamental mode formed in the slot generally increases linearly. The sensitivity was evaluated using



(a)

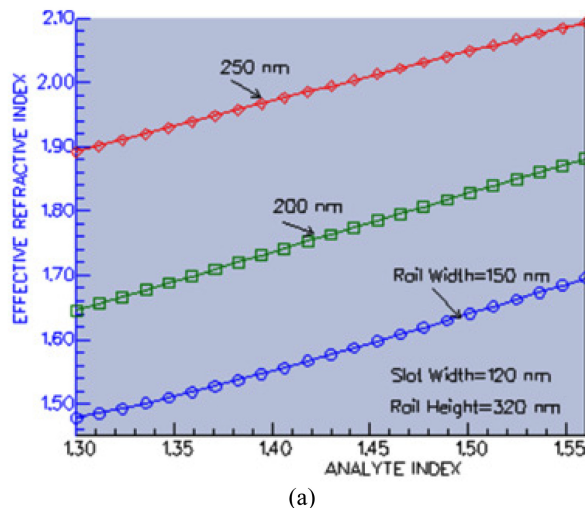


(b)

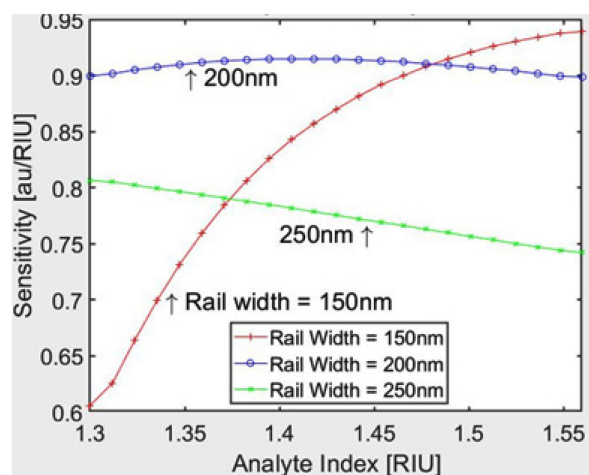
**Fig. 11.** Changes in the (a) effective refractive index of the TE mode and (b) waveguide sensitivity with an increase in the analyte refractive index for various slot widths (rail width = 200 nm; rail height = 320 nm).

Eq. (11) based on the rate of change in the effective refractive index. As shown in Fig. 11(b), in the case of a slot width of 120 nm, the deviation of the sensitivity was evaluated at a level of about 0.015 [au/RIU]. Although the 80 nm and 160 nm slot widths show higher sensitivities in a specific refractive index section, the small deviation in sensitivity in the overall sensing range is more important for the evaluation of sensor performance. Therefore, when the numerical value and deviation of the sensitivity are considered at the same time, the optimized slot width is considered to be 120 nm. Furthermore, it confirmed that a high confinement factor can be achieved with the slot width selected in the optimization process.

Next, the slot width and rail height were set to 120 nm and 320 nm, respectively, and the refractive index of the analyte was increased from 1.3 to 1.55 for rail widths of 150 nm, 200 nm, and



(a)



(b)

**Fig. 12.** Changes in the (a) effective refractive index of the TE mode and (b) waveguide sensitivity with an increase in the analyte refractive index for various rail widths (slot width = 120 nm; rail height = 320 nm).

250 nm; then, the change in the effective refractive index was analyzed. As shown in Fig. 12(a), as the refractive index of the analytes increases, the effective refractive index of the fundamental mode generally increases linearly. In this case, the sensitivity was also evaluated, and as shown in Fig. 12(b), the deviation in the sensitivity was evaluated as less than approximately 0.01 [au/RIU] for a rail width of 200 nm. Therefore, even in this case, it can be confirmed that the rail width of 200 nm selected in the optimization process results in a high confinement factor.

The change in the effective refractive index of the fundamental mode was analyzed when the slot and rail widths of the optimized slot optical waveguide were set to 120 nm and 200 nm, respectively, and the refractive index of the analyte was varied within the range of 1.3-1.55 for rail heights of 240 nm, 320 nm, and 370 nm. As shown in Fig. 13(a), as the refractive index of the

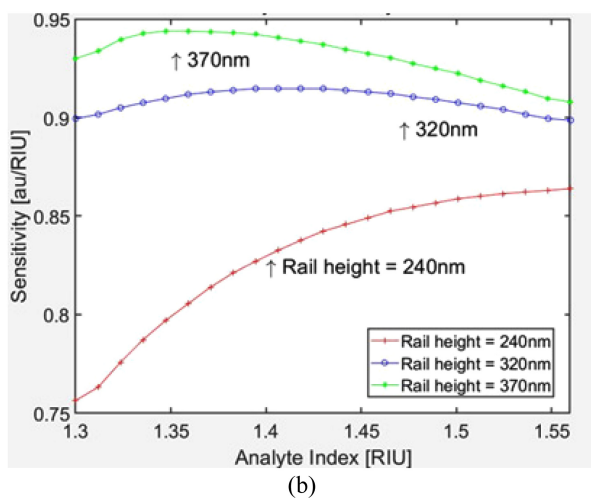
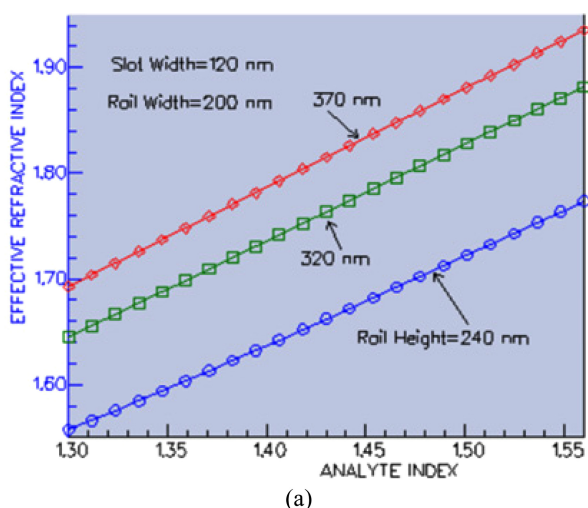


**Fig. 13.** Changes in the (a) effective refractive index of the TE mode and (b) sensitivity with an increase in the analyte refractive index for various rail heights (slot width = 120 nm; rail width = 200 nm).

analytes increases, the effective refractive index of the fundamental mode generally increases linearly. The sensitivity was also evaluated, as shown in Fig. 13(b), and the deviation in the sensitivity was evaluated as 0.03 [au/RIU] for a 320 nm rail width.

The confinement factor was comprehensively evaluated based on the ratio of a fundamental mode distributed in the slot. Furthermore, the effective refractive index of the fundamental mode based on the refractive index of the analyte in the slot and the sensitivity were evaluated. The same results were achieved by using both approaches: when the slot width, rail width, and height were set to 120 nm, 200 nm, and 320 nm, respectively, the confinement factor was evaluated as -56% and the waveguide sensitivity was -0.9 [au/RIU] or higher. If the optimized slot optical waveguide is used as an integrated-optic biochemical sensor, excellent performance can be expected.

### 4.3 Surface Sensing

Surface sensing is based on the immobilization of a very thin layer of receptors on the bottom of the slot and the top surfaces of rail. The interaction between the analyte and receptor produces a change in the specific molecular ( $n_a$ ) adlayer thickness ( $t_a$ ), affecting the effective refractive index of the propagating optical mode, as shown in Fig. 14. By functionalizing the waveguide surface with specific receptors, sensing can be used for specific detection of certain analytes, such as antibody-antigens including biotin-streptavidin and prostate specific antigen (PSA)-bovine serum albumin (BSA), and pollutants in water. In this section, we focus on how the specifications of the slot waveguide affect the surfacing sensing using the quasi-TM mode, in which the dominant transverse magnetic field component is parallel to the surface of the slot and rail.

First, a computational analysis was performed on the modal effective refractive index for a 1-40 nm change in the thickness of

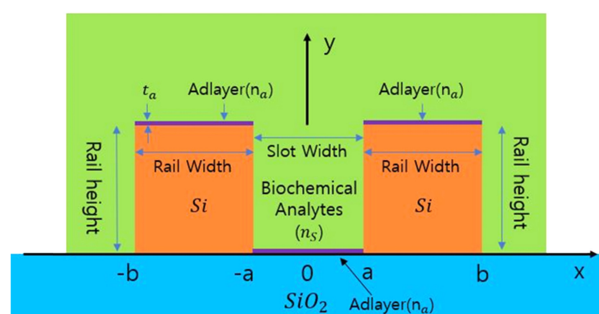


**Fig. 14.** Cross-sectional schematic of the vertical slot optical waveguide for computational analysis of surface sensing.

the sodium chloride layer and the sensitivity based on Eq. (11) was calculated as shown in Fig. 15. As the thickness of sodium chloride layer increases, the effective refractive index of the quasi-TM mode increases because the refractive index of sodium chloride is larger than that of the cover cladding material (water). On the other hand, the narrower the slot width in the computational analysis, the more difficult it is to drive a mode close to the TM. Therefore, it was confirmed that a slot width  $\geq 150$  nm is needed to obtain a quasi-TM mode  $\geq 90\%$ . As shown in Fig. 15(b), a sensitivity of approximately  $6-9 \times 10^{-4}$  [RIU/nm] can be achieved for a 150 nm slot width and a 2-40 nm thickness range. Meanwhile, Fig. 16 shows the effective refractive index and sensitivity according to the thickness of isopropanol, ethylene glycol, and sodium chloride materials for a slot, rail width, and rail

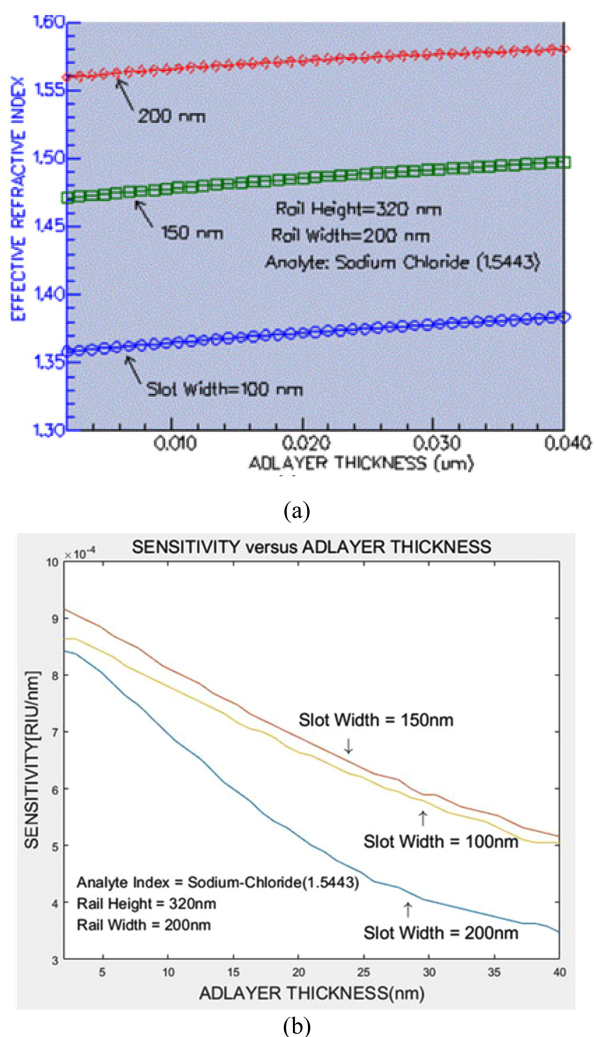


**Fig. 15.** Change in the (a) effective refractive index of the TM mode and (b) sensitivity with an increase in sodium-chloride thickness for various slot widths (rail width = 200 nm; rail height = 320 nm).

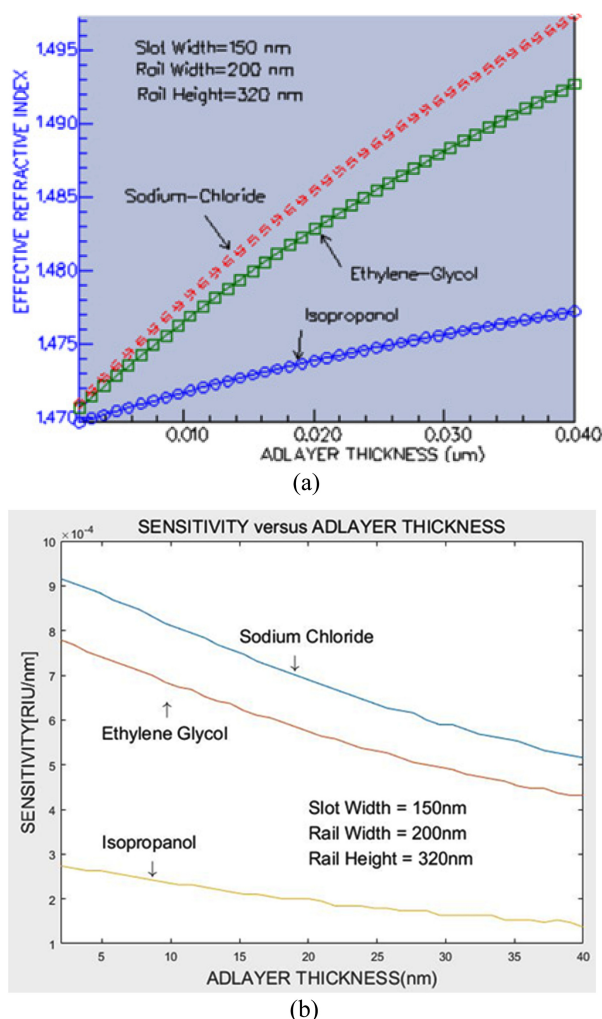


**Fig. 16.** Change in the (a) effective refractive index of the TM mode and (b) sensitivity with an increase in the layer thickness of the analyte for various materials (slot width = 150 nm; rail width = 200 nm; rail height = 320 nm).

height of 150 nm, 200, nm and 320 nm, respectively. In Fig. 16(b), it can be observed that, the smaller the refractive index of the analyte, the smaller the deviation of the sensitivity according to the thickness.

Fig. 17 show the change in the effective refractive index of the TM mode and sensitivity according to the thickness of the sodium-chloride layer for various rail widths and a slot width and rail height of 150 nm and 320 nm, respectively. By the way, Fig. 18 show the change in the effective refractive index of the TM mode and sensitivity according to the thickness of the sodium-chloride layer for various rail height and a slot width and rail width of 150 nm and 200 nm, respectively. It was confirmed that the change in sensitivity with changes in the rail width or height and analyte thickness was relatively small. The rail width and

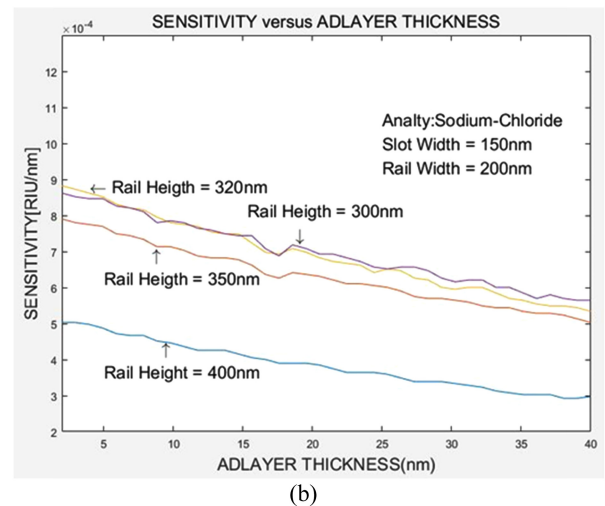
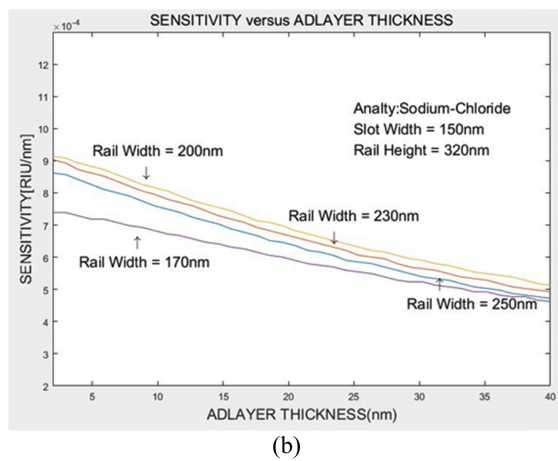
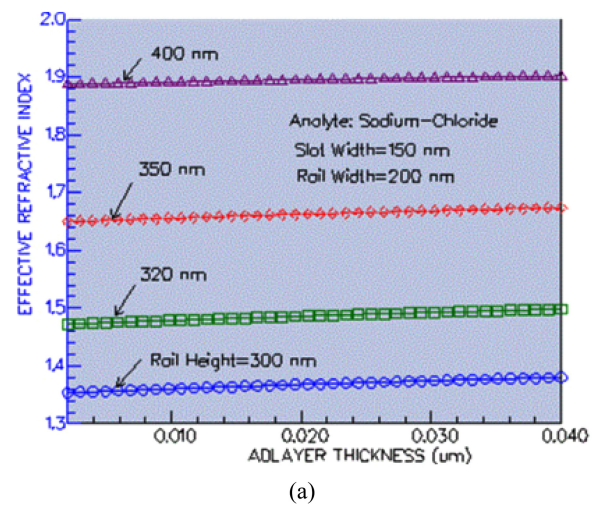
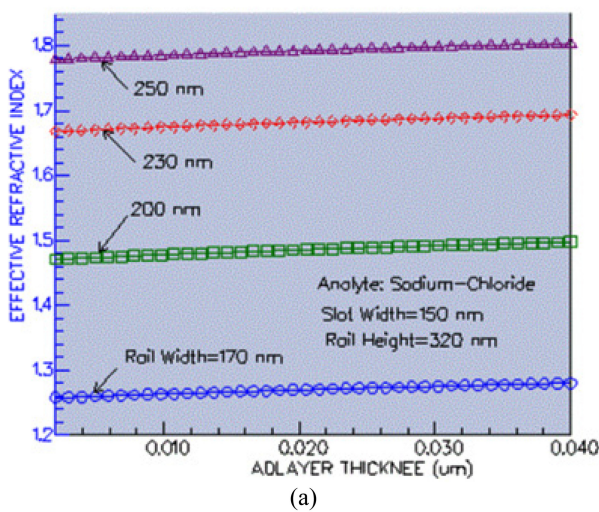


**Fig. 17.** Change in the (a) effective refractive index of the TM mode and (b) sensitivity with changes in the thickness of the sodium-chloride layer for various rail widths (slot width = 150 nm; rail height = 320 nm).

**Fig. 18.** Changes in the (a) effective refractive index of the TM mode and (b) sensitivity with changes in the thickness of the sodium-chloride layer for various rail heights (slot width = 150 nm; rail width = 200 nm).

height of 200 nm and 320 nm, respectively, show the smallest deviations in the sensitivities, as shown in Fig. 17(b) and Fig. 18(b), as we expect. Therefore, even in this case, it can be confirmed that the rail width and height of 200 nm and 320 nm, respectively, selected in the optimization process results in a high confinement factor.

## 5. CONCLUSIONS

The TE and TM mode field distributions in the SOI slot optical waveguide were analyzed analytically by applying boundary continuity conditions to the Maxwell wave equation. The optimized specifications of the slot optical waveguide suitable for the integrated optical biochemical sensor, that is, slot width, rail width, and height, were derived through numerical analysis based

on the confinement factor of the optical mode distributed in the slot. In addition, the effect of the optimized specifications on the transmission power was discussed.

The waveguide sensitivities of homogeneous and surface sensing were calculated based on the specifications of the optimized slot optical waveguide. The confinement coefficient and waveguide sensitivity for homogeneous sensing and the TE mode were evaluated as approximately 56% and 0.9 [au/RIU], respectively, for the slot width, rail width and height which were set to 120 nm, 200 nm, and 320 nm. The waveguide sensitivity for surface sensing and the TM mode was evaluated as  $(3-9) \times 10^{-4}$  [RIU/nm] in the analyte refractive index range of 1.37-1.5443 and thickness range of 2-40 nm. Therefore, excellent sensing performance can be expected when an integrated-optic biochemical sensor is implemented by applying an optimized

vertical slot optical waveguide to a Mach-Zehnder interferometer, modal interferometer, and ring resonator.

## ACKNOWLEDGMENT

This research was supported by the Basic Science Research Program (2018R1D1A1B07049908) through the National Research Foundation of Korea (KNRF), funded by the Ministry of Science and ICT. This study was conducted during the sabbatical period.

## REFERENCES

- [1] X. Fan, I. White, S. Shopova, H. Zhu, J. Suter and Y. Sun, "Sensitive optical biosensors for unlabeled targets: A review", *Analytica Chimica Acta.*, Vol. 620, No. 1-2, pp. 8-26, 2008.
- [2] R. Chandrasekar, Z. J. Lapin, A. S. Nichols, R. M. Braun and A. W. Fountain, "Photonic integrated circuits for Department of Defense-relevant chemical and biological sensing applications: state-of-the-art and future outlooks", *OE.*, Vol. 58, No. 2, pp. 0220901(1)-0220901(11), 2019.
- [3] F. Prieto, B. Sepulveda, A. Calle, A. Llobera, C. Dominguez, A. Abad, A. Montoya, and L. M. Lechuga, "An integrated optical interferometric nanodevice based on silicon technology for biosensor applications", *Nanotechnology*, Vol. 14, No. 8, pp. 907-912, 2003.
- [4] E. Luan, H. Shoman, D. M. Ratner, K. C. Cheung and L. Chrostowski, "Silicon Photonics Biosensors Using Label-Free Detection", *Sensors*, Vol. 18, No. 10, pp. 3019(1)-3019(4), 2018.
- [5] F. Brosinger, H. Freimuth, M. Lacher, W. Ehrfeld, E. Gedig, A. Katerkamp, F. Spener and K. A. Cammann, "Label-free affinity sensor with compensation of unspecific protein interaction by a highly sensitive integrated optical Mach-Zehnder interferometer on silicon. Sens", *Actuators B*, Vol. 44, No. 1-3, pp. 350-355, 1997.
- [6] P. Munoz G. Micó, L. A. Bru, D. Pastor, D. Pérez, J. D. Doménech, J. Fernández, R. Baños, B. Gargallo, R. Alemany, A. M. Sánchez, J. M. Cirera, R. Mas, and C. Dominguez, "Silicon Nitride Photonic Integration Platforms for Visible, Near-Infrared and Mid-Infrared Applications", *Sensors*, Vol. 17, No. 9, pp. 2088(1)-2088(25), 2017.
- [7] K. Worhoff, R. G. Heideman, A. Leinse, and M. Hoekman, "TriPlex: a versatile dielectric photonic platform", *Adv. Opt. Techn.*, Vol. 4, No. 2, pp. 189-207, 2017.
- [8] D. J. Blumental, R. Heidman, D. Geuzberoeck, A. Leinse and C. Roeloffzen, "Silicon Nitride in Silicon Photonics", *Proc. IEEE*, Vol. 106, No. 12, pp. 2209-2231, 2018.
- [9] K. Zinoviev, A. B. Gonzalez-Guerrero, C. Dominguez and L. M. Lechuga, "Integrated Bimodal Waveguide Interferometric Bio-sensor for Label-Free Analysis", *J. Lightwave Technol.*, Vol. 29, No. 13, pp. 1926-1930, 2011.
- [10] V. R. Almeida, Q. Xu, C. A. Barrios, and M. Lipson, "Guiding and confining light in void nanostructure", *Opt. Lett.*, Vol. 29, No. 11, pp. 2395-2398, 2004.
- [11] T. Baehr-Jones, M. Hochberg, C. Walker, and A. Scherer, "High-Q optical resonator in silicon-on-insulator-based slot waveguides", *Appl. Phys. Lett.*, Vol. 86, No. 8, pp. 081101(1)-081101(3), 2005.
- [12] N. N. Feng, J. Michel and L. C. Kimerling, "Optical Field Concentration in Low-Index Waveguides", *IEEE J. Quant. Elec.*, Vol. 42, No. 9, pp. 883-888, 2006.
- [13] P. Steglich, *Silicon-on-Insulator Slot Waveguides: Theory and Applications in Electro-Optics and Optical sensing*, Emerging Waveguide Technology, IntechOpen. pp. 187-210, London, United Kingdom, 2018.
- [14] C. Koos, P. Vorreau, T. Vallaitis, P. Dumon, W. Bogaerts, R. Baets, B. Esembeson, I. Biaggio, T. Michinobu, F. Diederich, W. Freude, and J. Leuthold, "All-optical high-speed signal processing with silicon-organic hybrid slot waveguides", *Nat. Photonics*, Vol. 3, No. 4, pp. 216-219, 2009.
- [15] M. Roussey, L. Ahmadi, S. Péliisset, M. Häyriinen, A. Bera, V. Kontturi, J. Laukkanen, I. Vartiainen, S. Honkanen, and M. Kuittinen, "Strip-loaded horizontal slot waveguide", *Opt. Lett.*, Vol. 42, No. 2, pp. 211-214, 2017.
- [16] H. Zengzhi, Y. Zhang, C. Zeng, D. Li, M. S. Nisar, J. Yu, and J. Xia, "High Confinement Factor Ridge Slot Waveguide for Optical Sensing", *IEEE Phot. Technol. Lett.*, Vol. 27, No. 22, pp. 2395-2398, 2015.
- [17] R. Singh and V. Priye, "Si<sub>3</sub>N<sub>4</sub>-SiO<sub>2</sub> Based Curve Slot Waveguide for High Confinement Factor and Low Mode Effective Area along with Biosensing Application", *Silicon*, pp. 1-9, 2021.
- [18] C. A. Barrios, "Optical Slot-Waveguide Based Biochemical Sensors. Sensors", Vol. 9, No. 6, pp. 4751-4765, 2009.
- [19] Q. Xu, V. R. Almeida, R. R. Panepucci and M. Lipson, "Experimental demonstration of guiding and confining light in nanometer-size low-refractive-index material", *Opt. Lett.*, Vol. 29, No. 4, pp. 1626-1628, 2004.
- [20] T. Baehr-Johnes, T. Baehr-Jones, M. Hochberg, Guangxi Wang, R. Lawson, Y. Liao, P. A. Sullivan, L. Dalton, A. K.-Y. Jen, and A. Scherer, "Optical modulation and detection in slotted silicon waveguides", *Opt. Express*, Vol. 13, No. 14, pp. 5216-5226, 2005.
- [21] Q. Liu, X. Tu, K. W. Kim, J. S. Kee, Y. Shin, K. Han, Y. J. Yoon, G. Q. Lo, and M. K. Park, "Highly sensitive Mach-Zehnder interferometer biosensor based on silicon nitride slot waveguide", *Sens. Act. B: Chem.*, Vol. 188, No. 11, pp. 681-683, 2013.
- [22] C. A. Barrios and M. Lipson, "Electrically driven silicon resonant light emitting device based on slot-waveguide", *Opt. Express*, Vol. 13, No. 25, pp. 10092-10101, 2005.
- [23] T. Fuisisawa and M. Koshiba, "Polarization-independent optical directional coupler on slot waveguides", *Opt. Lett.* Vol. 31, No. 1, pp. 56-58, 2006.
- [24] T. Fuisisawa, and M. Koshiba, "All-optical logic gates based on nonlinear slot-waveguide couplers", *J. Opt. Soc. Am.*, Vol. 23, No. 4, pp. 684-691, 2006.
- [25] T. Fuisisawa and M. Koshiba, "Theoretical Investigation of

- Ultrasmall Polarization-Insensitive 1x2 Multimode Interference Wave-guide Based on Sandwiched Structures”, *IEEE Photon. Technol. Lett.*, Vol. 18, No. 11, pp. 1246-1248, 2006.
- [26] P. Mullner and R. Hainberger, “Structural Optimization of Silicon-On-Insulator Slot Waveguides”, *IEEE Photon. Technol. Lett.*, Vol. 18, No. 24, pp. 2557-2559, 2006.
- [27] F. Dell’Olio, and V. N. N. Passaro, “Optical sensing by optimized silicon slot waveguides”, *Opt. Express*, Vol. 15, No. 8, pp. 4977-4993, 2007.
- [28] J. Milvich, D. Kohler, W. Freude and C. Koos, “Surface sensing with integrated optical waveguides: a design guideline”, *Opt. Express*, Vol. 26, No. 16, pp. 19885-19906, 2018.
- [29] Photon Design Ltd., *FIMMWAVE v6.6.0*, Oxford, United Kingdom, 2018.
- [30] Photon Design Ltd, *FIMMPROP v6.6.0*, Oxford, United Kingdom, 2018.
- [31] Y. Liu, M. Kong, and Y. Jiang, “Transverse magnetic modes in planar slot waveguides”, *J. Opti. Soci. B Am.*, Vol. 32, No. 10, pp. 2052-2060, 2015.
- [32] Y. Jiang, M. Kong, C. Liu, Y. Liu and Y. Wang,” Transverse electric modes in planar slot waveguides”, *J. Modern Optics*, Vol. 65, No. 1, pp. 111-118, 2018.
- [33] Y. Fan, S. Peng, and Y. Liu, “Transverse magnetic modes in hybrid nanoslot waveguides”, *Results in Physics*, Vol. 16, No. 3, pp. 103017(1)-103017(9), 2020.
- [34] J. G.Wanguemert-Perez, A. Hadij-ElHouati, A. Sánchez-Postigo, J. Leuermann, D. X. Xu, P. Cheben, A. Ortega-Moñux, Robert Halir, and Í. Molina-Fernández, “Subwavelength structures for silicon photonics biosensing”, *Opt Laser Technol.*, Vol. 109, No. 1, pp. 437-448, 2019.
- [35] T. Taniguchi, A. Hirowatari, T. Ikeda, M. Fukuyama, Y. Amemiya, A. Kuroda, and S. Yokoyama, “Detection of antibody-antigen reaction by silicon nitride slot-ring biosensors using protein G”, *Opt. Commun.*, Vol. 365, No. 4, pp. 16-23, 2016.